



LAWRENCE
LIVERMORE
NATIONAL
LABORATORY

Equilibrium and vertical-instability considerations for vertical strike-point shifts on the ITER divertor targets.

R. A. Kolesnikov, R. H. Bulmer, L. L. LoDestro, T. A. Casper, R. A. Pitts

August 22, 2013

Nuclear Fusion

Disclaimer

This document was prepared as an account of work sponsored by an agency of the United States government. Neither the United States government nor Lawrence Livermore National Security, LLC, nor any of their employees makes any warranty, expressed or implied, or assumes any legal liability or responsibility for the accuracy, completeness, or usefulness of any information, apparatus, product, or process disclosed, or represents that its use would not infringe privately owned rights. Reference herein to any specific commercial product, process, or service by trade name, trademark, manufacturer, or otherwise does not necessarily constitute or imply its endorsement, recommendation, or favoring by the United States government or Lawrence Livermore National Security, LLC. The views and opinions of authors expressed herein do not necessarily state or reflect those of the United States government or Lawrence Livermore National Security, LLC, and shall not be used for advertising or product endorsement purposes.

Equilibrium and vertical-instability considerations for vertical strike-point shifts on the ITER divertor targets.

R. A. Kolesnikov, R. H. Bulmer, L. L. LoDestro
Lawrence Livermore National Laboratory, Livermore, CA, USA

T. A. Casper, R. A. Pitts
ITER Organization, France
(Dated: June 18, 2013)

The study of operation with raised strike-points on the first ITER divertor target plates is motivated by the need to gain experience with operation with strike-points on tungsten (W) surfaces during the non-active phases (in the case of an initial CFC/W divertor); or (if ITER begins with a full-W divertor), to gain experience with plasma control and transients while operating with raised strike-points to avoid damaging the baseline strike regions in preparation for the nuclear phase, and to provide a means for operation should damage occur in the baseline strike zone. For operation with raised strike-points, we use the Corsica code to investigate the range of possible H- and L-mode equilibria, with emphasis on the maximum plasma current, achievable shapes, etc. With raised strike-points the maximum achievable plasma current is close to 14 MA. The operating space ($\beta_p - l_i$) for raised strike point has been studied. The size of the $\beta_p - l_i$ operating space shrinks (compared to using standard strike point positions) at 14 MA. For 12 MA however, the operation space is not affected when using raised strike points. For equilibria with elevated strike-points (at roughly the CFC/W transitions, following the 2007 ITER Design Review) the vertical-instability growth-rates at high plasma current (14 MA) are somewhat high but are within the 20 s^{-1} which studies indicate are controllable in ITER. At lower currents (12 MA) in H-mode, the vertical-instability growth-rates stay below 10.0 s^{-1} for most of $\beta_p - l_i$ space. At 12 MA in H-mode, multiple equilibria which meet our constraints have been found in overlapping regions of the $\beta_p - l_i$ operating space.

PACS numbers: 52.25.Xz, 52.55.Fa, 52.55.Rk

I. INTRODUCTION

In the reference ITER divertor strategy, carbon fibre composite (CFC) is planned for the plasma-facing material in the high-heat-flux regions throughout the non-active (hydrogen-helium) campaigns [1]. This baseline ‘first’ divertor, shown in Fig. 1, comprises inner and outer targets with CFC monoblocks in the ‘straight’, mostly vertical parts of each plate, and a transition to tungsten (W) monoblocks for the curved, or ‘baffle’ zones. This divertor is to be replaced by a full-W variant before nuclear operations begin [1]. The key drivers of this strategy are avoidance in the nuclear phase of the expected high levels of fuel retention by co-deposition associated with carbon and the provision of a more forgiving material in the initial phases of operation, when scenarios will require development, including plasma control and techniques for disruption and ELM avoidance and mitigation [1].

Even at relatively low plasma current I_p and input power, ITER plasmas will have significantly higher stored energy than the largest of today’s tokamaks. Tungsten melts, unlike carbon, and melting is expected to be possible during non-active operations [2]. A number of recent studies have demonstrated that divertor operation on topologically-damaged W surfaces can be difficult, if not impossible (see, e.g., [3]), due essentially to the fact that once surface damage begins, subsequent operation simply amplifies the problem [4]. Beginning operations

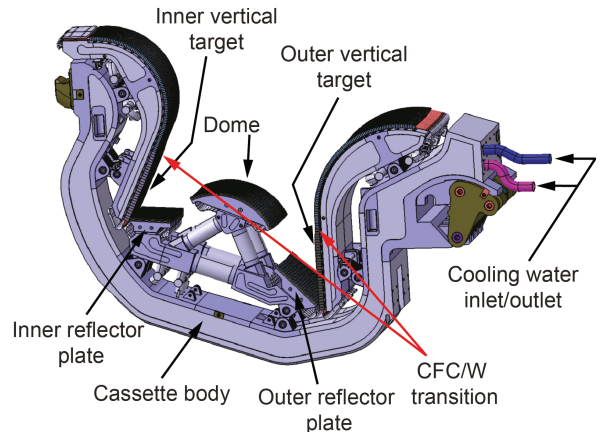


FIG. 1: First ITER divertor (according to the 2007 ITER design review). Components of the divertor are illustrated including inner and outer vertical targets (with CFC/W transitions) as well as reflector plates and the dome.

with CFC at the strike zones (around the strike points, i.e., where the ‘legs’ of the plasma’s equilibrium separatrix strike the divertor) is thus a low-risk strategy, benefitting in addition from the very substantial experience of operation with carbon plasma-facing components which has been accumulated in the tokamak community. Raising the strike points to allow operation at some maximum value of I_p fully on W surfaces was the motivation, dur-

ing the 2007 ITER Design Review, for a lowering (by 10 cm) of the CFC/W transition on the vertical targets. This would allow some experience to be gained before the switch to full W prior to the first nuclear campaigns [1]. At the time, only very approximate studies of the highest possible I_p with raised strike-points had been made. This paper reports on the results of a more complete study of the operational space allowed by the ITER coil set in this case.

A further important motivation for this raised strike-point study is the proposal in late 2011 by the ITER Organization to abandon the first CFC/W divertor and begin operations with a full-W variant [2]. This new strategy, the result of cost-containment measures, was supported by the ITER Council, subject to a period of R&D aiming to quantify as far as possible the physics/operational risks and to demonstrate the availability of the required W monoblock technology. A decision on the proposal is expected around the end of 2013.

If ITER does begin operations with a full-W divertor, this divertor must by definition survive until well into the nuclear phase. Operation with raised strike-points is then one approach with which areas which have been damaged can be avoided. Depending on the levels of damage, this may well be mandatory for operations to continue, even in non-active phases. Alternatively, future operators may decide to test scenarios, and gain experience with mitigation techniques, using raised strike-points to avoid damaging the strike regions that are required for planned baseline 15 MA operations.

Finally, a degree of strike-point sweeping may be required for diagnostic purposes (for example mapping of target profiles using embedded Langmuir probes or studying the 2D structure of the divertor plasma with divertor Thomson Scattering). This option is of course independent of which divertor material combination is in place.

In this paper we explore the domains of operation possible with raised strike-points for equilibria at the Start-of-Burn (SOB). We use the Corsica free-boundary code [5, 6] to investigate the $\beta_p - l_i$ operating space accessible for the present divertor design with elevated strike-points. We begin with elevated positions roughly equivalent to the CFC/W transition points following the 2007 ITER Design Review (vertical positions $Z_{\text{el0}}^{\text{in}} = -3.35$ m and $Z_{\text{el0}}^{\text{out}} = -3.90$ m on the inner and outer divertor targets, respectively). For comparison, the baseline vertical positions are $Z_{\text{base}}^{\text{in}} = -3.79$ m and $Z_{\text{base}}^{\text{out}} = -4.406$ m on the inner and outer divertor targets, respectively. We consider configurations close to the maximum plasma current consistent with coil and other constraints (Sec. III A), as well as with intermediate plasma current (Sec. III B). As the strike-point locations are varied (lowered from $Z_{\text{el0}}^{\text{in,out}}$ and raised to a maximum roughly equivalent to where it would have been above $Z_{\text{el0}}^{\text{in,out}}$ for the CFC/W divertor), the maximum achievable plasma current is determined (Sec. IV). Additionally, we report the resulting vertical-instability growth-rates, a primary

measure of the controllability of the plasmas by the position and shape control system [7, 8].

In the course of our simulations, we require certain physics and engineering constraints to be met by our solutions to the Grad-Shafranov equation. For all equilibria reported here, the following constraints are satisfied: $q_0 \geq 0.95$. Although operation at $q_{95} < 3$ is possible, in this work we constrain $q_{95} \geq 3$. The vacuum toroidal field is 5.3 T at major radius $R = 6.2$ m. Superconducting poloidal field (PF) and central solenoid (CS) coil limits ($I - B$ limit-line and limits on the net and repulsive CS coil forces) are met; and minimum SOL-wall distances in the outboard and inboard half-planes [9] are observed.¹ In our simulations we always make sure that the upper null (non-active X-point) is located outside the first-wall plasma-facing surface (see Figs. 2–3). (Additional physics/engineering constraints are imposed during various scans and will be described as they arise.)

In order to implement a given set of physics/engineering constraints, various specifications of numerical constraints are possible. For instance, the steepness of the radial current profile (a variable in the numerical constraint set) can be varied to enforce either $\max(U)$ or q_{95} [see Eq. (3) and the definitions in Sec. II]. We find that in the lower-current regime, different regions of $\beta_p - l_i$ operating space are better surveyed (i.e., the extent of $\beta_p - l_i$ in which solutions exist will be larger) using different sets of constraints, with these regions partially overlapping. In these overlapping regions different equilibria are found at the same β_p and l_i . We consider the existence of multiple equilibria satisfying our physics/engineering constraint set a favorable result (see discussion in Secs. III B and IV).

II. DEFINITION OF VARIABLES AND CONSTRAINTS

In this section we introduce the variables and profile shapes used in the simulations, as well as a few constraints beyond those just mentioned above. In addition, we describe our techniques for controlling the separatrix in our free-boundary Grad-Shafranov solver, which are needed to satisfy the particular sets of constraints on SOL-wall distance, plasma shape, strike-point locations, etc.

¹ The last constraint states that the minimum distance between the SOL outer surface and the first wall must be at least 8 cm in both the inboard and outboard half-planes. The SOL is defined here to be the volume between the active separatrix and the flux surface which is located 4 cm away from it at the outer mid-plane. Also, the SOL must lie within the inactive separatrix. This leads to the constraint $dR_{\text{sep}} \geq 4$ cm, where dR_{sep} is the distance between the active and inactive separatrices at the outer mid-plane.

The ITER definitions of poloidal beta β_p and normalized internal inductance l_i (in SI units) are used in this paper:

$$\beta_p = \frac{2\mu_0 \langle \langle p \rangle \rangle}{\langle B_p^2 \rangle|_{\text{bound}}}, \quad (1)$$

$$l_i = \frac{2V \langle \langle B_p^2 \rangle \rangle}{R_0(\mu_0 I_p)^2}. \quad (2)$$

Here V is plasma volume, I_p is the plasma current, R_0 is the major radius and B_p is the poloidal magnetic field; $\langle \langle \rangle \rangle$ indicates a volume average, while $\langle \rangle|_{\text{bound}}$ indicates the flux-surface average at the plasma boundary.²

The plasma current and pressure radial profiles for all equilibria in this paper are given by:

$$J_O(x) = c_0 \begin{cases} 1, & 0 < x \leq x_s; \\ \left(1 - x_0^{b_J}\right)^{a_J} + \Delta_J, & x_s < x \leq 1. \end{cases} \quad (3)$$

$$p(x) = c_0 \beta_J \begin{cases} 1, & 0 < x \leq x_s; \\ \left(1 - x_0^{b_p}\right)^{a_p} + \Delta_p, & x_s < x \leq 1. \end{cases} \quad (4)$$

The current profile J_O is used together with p' to calculate FF' for the Grad-Shafranov equation [5] and the normalization constant c_0 is determined by I_p . Here $x_0 \equiv (x - x_s)/(1 - x_s)$ and $x \equiv (\psi - \psi_{\text{axis}})/(\psi_{\text{bound}} - \psi_{\text{axis}})$ with ψ being poloidal flux; ψ_{axis} and ψ_{bound} are fluxes on the magnetic axis and plasma boundary, respectively; and x_s defines a sawtooth region. In L-mode, $\Delta_J = 0$ and $\Delta_p = 0$, while in H-mode

$$\Delta_i = \epsilon_i C_i (1 - x_0)^{k_i} x_0^{\eta_i}, \quad C_i = (1 + \eta_i)^{1 + \eta_i} / \eta_i^{\eta_i}. \quad (5)$$

Here $i = J, p$ with the parameters listed in the following table:

TABLE I: List of Parameters

	$i = J$	$i = p$
ϵ	0.25	0.07
a	varied	2
b	2	1
η	-20	-10
k	1	2

In our survey we used a_J , β_J and x_s as adjustable parameters to meet constraints. For the higher- l_i equilibria, q_0 on the axis is enforced to be equal to 0.95 by varying the sawtooth region x_s . At lower l_i , $x_s = 0$ and q_0 is allowed to float above 0.95.

In representing the fiducial states of a scenario, the required flux-linkage $\langle \Psi_{\text{ext}} \rangle$ (plasma-current-weighted

poloidal flux from the PF and CS coils linking the plasma) as well as the inductive flux consumption are found as a result of constraining the free-boundary Grad-Shafranov solution, while varying the CS and PF coil currents, to obey the following equation

$$\langle \Psi_{\text{ext}} \rangle = \Psi_{\text{init}} - L_p I_p - \mu_0 C_E I_p R_0. \quad (6)$$

Here L_p is the (calculated) plasma self-inductance and C_E is the Ejima coefficient modeling the resistive flux consumption (see, e.g., Refs. 10–12). Throughout this paper (as in Ref. 12) C_E is taken to be 0.3. The last two terms on the right-hand side of Eq. (6) are computed relative to an initiation point Ψ_{init} for a given phase of the scenario. For the baseline $I_p^{\text{base}} = 15$ MA SOB state, Ψ_{init} (input parameter) is estimated to be 106.6 Wb, which is equal to the initial magnetization flux (maximum poloidal flux capability of the system) minus the 8 Wb flux consumed during the plasma formation phase as well as the 3 Wb resistive flux consumed in the heating phase, i.e., between the Start-of-Flatop (SOF) and SOB. The resistive flux consumed during the current ramp-up is accounted for with the C_E term in Eq. (6). The input values for C_E and Ψ_{init} given above are estimates obtained from scenario simulations [13]. In particular, C_E of about 0.3 was obtained assuming a fast plasma-current ramp-up (during about 50 s) with low impurity content and auxiliary heating after early formation of the diverted configuration. $C_E = 0.3$ is the expected lower level of resistive losses of the magnetic flux. Increasing, for example, the plasma-current ramp-up time or reducing the auxiliary heating will increase C_E .

When operating at different plasma currents, in taking into account the CS coil system's contribution to plasma shaping, we reduce Ψ_{init} by $14(I_p^{\text{base}} - I_p)$ for optimal use of PF coil resources (the coefficient is $L_p + \mu_0 C_E R_0$, where L_p is calculated using the baseline SOB equilibrium [12]).

The critical states in ITER scenarios with respect to the plasma-shaping capability of the coil set are SOF and SOB. We survey here only SOB equilibria, but by considering a wide range of β_p at SOB we essentially cover the SOF state as well. There will be some additional effects at the End-of-Burn (EOB), but with the plasma current reduced from its 15 MA baseline value, the flatop capability is expected to be naturally extended. The flatop period itself is not a critical issue.

In the simulations, in addition to I_p and the profile parameters mentioned above, we vary PF and CS coil currents (Fig. 2) in order to satisfy Eq. (6) and to control the separatrix shape in the free-boundary Grad-Shafranov solution. In the figure, coils 13 and 14 are the in-vessel copper coil pair (VS3) added following the 2007 Design Review for improved vertical stability control. The remaining in-vessel coils constitute an axisymmetrized model of the ELM control system [14]. In Cor-

² These definitions for β_p and l_i have appeared elsewhere in the literature as $\beta_p(1)$ and $l_i(3)$.

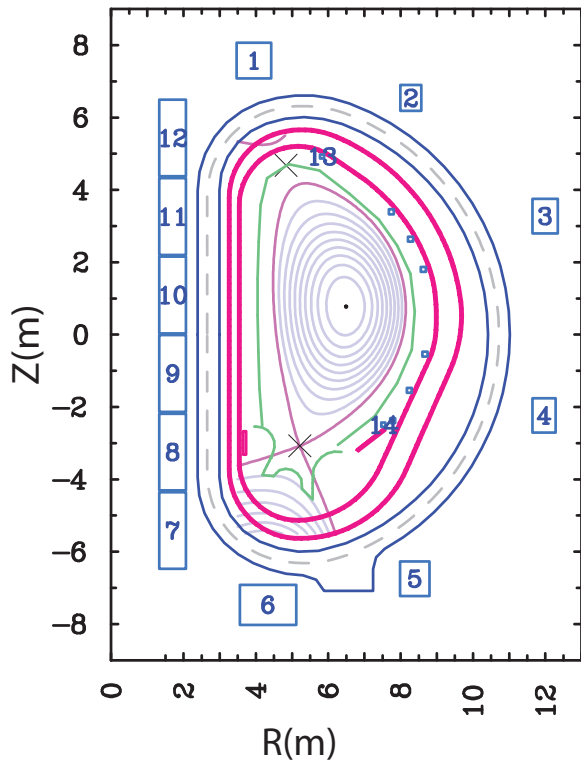


FIG. 2: Output from the Corsica code for an ITER equilibrium. Red lines represent the containment vessel and plates. Green lines represent the divertor and first-wall plasma-facing surface. Dark-blue double lines show toroidal magnetic-field coils. Light-blue rectangles show coils numerated clockwise (1 through 6 are PF coils, while 7 through 12 are CS coils). In this paper, only coils 1 through 12 carry current.

sica, the PF and CS coil currents³ are varied in order to force the plasma boundary to go through a finite number of ‘fixed’ points (e.g., points 1–4 shown in Fig. 3 with black circles). The coil currents are also used to match the active ‘fuzzy’ boundary points in the least-squares sense (only the pink plus-signs in the figure are active, i.e., have a non-zero weight attached to them. The fuzzy points with bigger weights are given higher priority in the least-squares matching procedure). The optimization can be done with different objective functions, such as including the sum of the squared coil currents or the sum of the magnetic field at the coils (although we find that equilibria tend to be near the high- B side of the superconducting limit-line). In all equilibria reported in this paper, we have adjusted the two lower fixed points to enforce the vertical positions of the strike-points on the divertor plates (points 3 and 4 in Fig. 3).

³ Neither VS3 nor the ELM control coils carry any current in this paper. The vacuum vessel and plates (shown in red in Fig. 2) are assumed to carry zero current in the equilibria, but they enter in the linear vertical-stability calculation.

The utilization factor U for a superconducting coil is a measure of its operating-point (in the $I-B$ plane) distance from the origin normalized to the limit-line distance from the origin. Thus, $U < 1$ indicates a coil is within its allowed operating space; $U = 1$ indicates a coil is at its operational limit; and $U > 1$ means a coil is above its allowed range. Constraining $\max(U) = 1$ makes sure that at least one of the coils is at its operational limit, with the rest of the coils being within the allowed space.

We define f to be the ratio of the U of the PF6 coil over the maximum of the net and repulsive CS coil forces (normalized to their maximum allowed values). Constraint $f = 1$ aims to maximize both U and one of the coil forces to effectively use coil resources.

III. OPERATING SPACE WITH ELEVATED STRIKE-POINTS

In this section we explore the domains of operation possible with strike-points raised on the divertor plates from their baseline positions. In Fig. 3, we show a typical example of a converged equilibrium with elevated strike-points in the 15 MA ITER baseline-scenario boundary. The magenta separatrix, found from the simulation, has been constrained to go through the elevated strike-points located vertically at $Z_{\text{el0}}^{\text{in,out}}$ as well as through points 1 and 2. The gray curve shows the inactive separatrix with the upper X-point.

In the following subsections, Secs. III A–III C, we study four configurations: baseline strike-points in L- and H-mode as well as raised strike-points in L- and H-mode. The complete sets of constraints for the various scans that follow are described in the Appendix. Note that we have looked at the operating space from the static-equilibrium point of view; therefore very large β_p (up to 0.8 and 0.9 for our L- and H-mode profiles, respectively) are seen in the figures; of course, time-dependent heating and current drive, transport, and stability considerations will significantly limit the range of possible β_p .

A. 14 MA operating space

With our equilibrium code we have found that I_p slightly above 14 MA is achievable in H-mode for the elevated-strike-points design (strike-points at $Z_{\text{el0}}^{\text{in,out}}$). To explore high-current operating space, we fix the plasma current to be equal to 14 MA. In Fig. 4, with L-mode regions located between the blue lines and H-mode regions located between the red lines, we show the extent of possible operating l_i space when β_p is varied from 0.1 to 0.9. The baseline strike-points configuration (given by the dashed lines) is compared to the elevated-strike-points configuration (given by the solid lines). When the strike-points are raised, the operating space shrinks (the apparent exception in L-mode at low l_i will be discussed shortly).

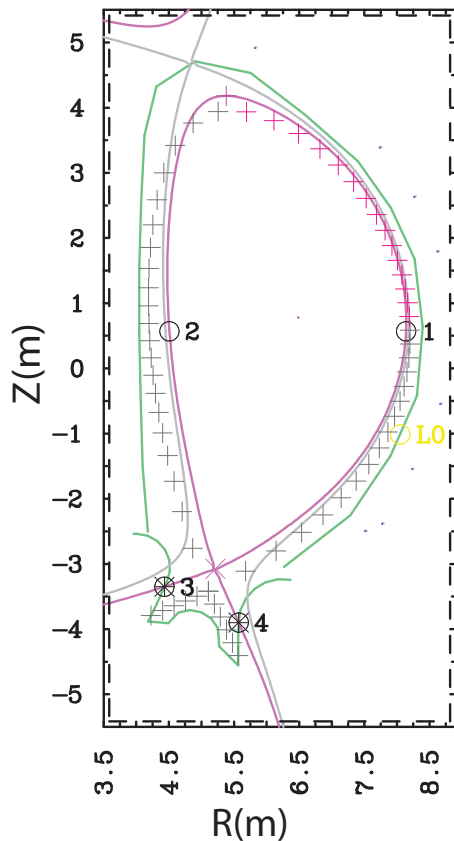


FIG. 3: Output from Corsica for an ITER equilibrium. Active (magenta) and non-active (gray) separatrixes are determined as part of the free-boundary solution. Locations of the active and inactive X-points are also shown by \times signs in Fig. 2. Plus-signs indicate the 15 MA baseline-scenario boundary. See text for further explanation.

To produce Fig. 4, we started with the baseline 15 MA SOB ITER equilibrium [12] with baseline β_p (0.7) and l_i (0.85) and originally located strike-points (at $Z_{\text{base}}^{\text{in,out}}$). Then we changed the current to 14 MA as well as adjusted the (average over plasma) initial flux Ψ_{init} from 106.6 to 92 Wb [see Eq. (6)]. Finally we generated 100 equilibria (10 in both the β_p and l_i directions) for each of the four cases (elevated and baseline strike-point configurations in both H- and L-modes). We next discuss some key features of the limits for each of the cases (again, the full set of constraints for each of the four cases is described in the Appendix).

For the *baseline strike-point configuration* (for both L- and H-modes; dashed lines in Fig. 4), the left limits are found when the $\max(U)$ reaches unity. The right limits are found when a balance occurs between the flattening (increasing x_s , which broadens the current profile and lowers q_0 and l_i) and peaking (increasing a_J , which narrows the current profile outside $x = x_s$ and raises l_i) of the current in the vicinity of the magnetic axis; we define a right limit when a_J reaches 10 since there is no noticeable change in the profile with further increase of a_J .

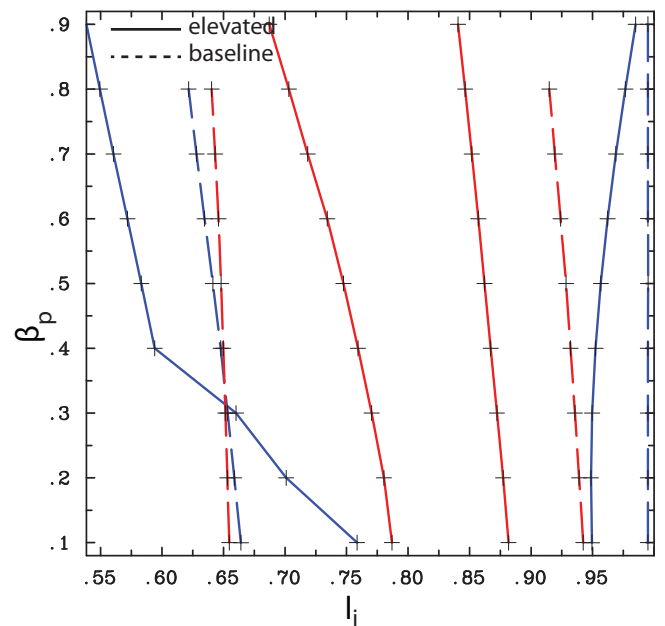


FIG. 4: The extent of achievable L-(blue) and H-mode (red) operating space (14 MA) in β_p and l_i (shown between pairs of lines) for both baseline (vertical positions are $Z_{\text{base}}^{\text{in}}$ and $Z_{\text{base}}^{\text{out}}$; dashed) and elevated-strike-point (vertical positions are $Z_{\text{el0}}^{\text{in}}$ and $Z_{\text{el0}}^{\text{out}}$; solid) configurations.

In L-mode when increasing l_i , the code stops converging before $a_J = 10$ is reached near $l_i = 1$; therefore the right limit (right dashed blue line) is defined to be $l_i = 1$ for simplicity.

For the *raised strike-point configuration* (Fig. 4; solid lines), the fixed points 3–4 enforce the vertical positions of the strike-points to be $Z_{\text{el0}}^{\text{in}}$ and $Z_{\text{el0}}^{\text{out}}$. The fixed points 1–2 are adjusted to enforce the minimum distances between the SOL and the first wall in the outboard and inboard half-planes to be equal to 8 cm.

In L-mode, the left limit of the raised strike-point operating space is found when q_{95} reaches its minimum ($q_{95} = 3$) for $\beta_p \leq 0.3$ and when the net CS coil force reaches its maximum (60.0 MN) for $\beta_p \geq 0.4$. The switch from q_{95} to a coil force limitation as β_p is increased explains the shape of the solid blue curve near $\beta_p = 0.4$.

For the raised strike-point configuration, the left limit of the H-mode operating space is found when $q_{95} = 3$, while the right limit is again found when the balance occurs between the flattening and peaking of the current on the axis.

Note that for $\beta_p > 0.3$, the low- l_i L-mode operating space with baseline strike-points is smaller than that with elevated strike-points. This is due to the fact that while $f = 1$ is enforced in our scan, this constraint is omitted with baseline strike-points. (Note that various specifications of the numerical constraints are possible—e.g., different parameters can be varied—to achieve the same set of physics constraints, as will be seen in Sec. III B below.

The most useful choice depends on the equilibrium— Z_{strike} , l_i , etc. The baseline curves in Fig. 4 were generated using the same numerical constraints as for the elevated-strike-point equilibria, and fail to converge when $f = 1$ is included. However, we expect that with another choice, e.g., the constraint-set used in Ref. 12, the $f = 1$ constraint could be included and the baseline operating space would then exceed that of the elevated-strike-point space.) Since the left L-mode elevated-strike-point limit for $\beta_p > 0.3$ is met when one of the coil forces is maximized, the $f = 1$ constraint ensures that the U of the PF6 coil is maximized as well; this helps effectively use coil resources and therefore increases the size of the operating space.

Fig. 5 shows the contours of the vertical-instability linear growth-rate γ (calculated using the linear vertical stability package [8] in Corsica) for 14 MA H-mode equilibria, for both baseline and elevated-strike-point configurations. With raising the strike-points (as well as with decreasing the initial flux Ψ_{init}), the growth rate increases; for typical $l_i = 0.85$ and $\beta_p = 0.7$, γ increases from 5.0 s^{-1} to 14.0 s^{-1} . If we look at corresponding equilibria (Fig. 3), when we start from a baseline boundary shown by the plus signs, as we raise the strike-points, the boundary (magenta curve) has a tendency to move away from the inboard wall. Note that for the raised-strike-point configuration the 8 cm distance between the SOL and the first wall is satisfied near the upper X-point throughout $\beta_p - l_i$ space. The resulting equilibria have higher elongation and consequently are more vertically unstable. For the raised strike-point configurations, γ varies between 12.5 s^{-1} and 18.0 s^{-1} at high and low β_p respectively (over the entire l_i operating space). These numbers are somewhat high but are within the 20 s^{-1} which studies indicate are controllable in ITER.⁴ Note that for 14 MA L-mode (not shown here), the growth rate again increases with elevating the strike-points, varying between 7.5 s^{-1} and 12.0 s^{-1} at high and low β_p , respectively.

B. 12 MA operating space

In Figs. 6–11, we investigate lower-plasma-current operation using the same profile shapes as described above. We select 12 MA for the study — a typical current for hybrid-mode scenarios being developed for ITER. (Note, however, that hybrid-mode profiles differ from the L- and H-mode model profiles given in Sec. II.) For 12 MA H-mode the size of the operating space is not affected much as we raise the strike-points to $Z_{\text{el0}}^{\text{in,out}}$. Operating at

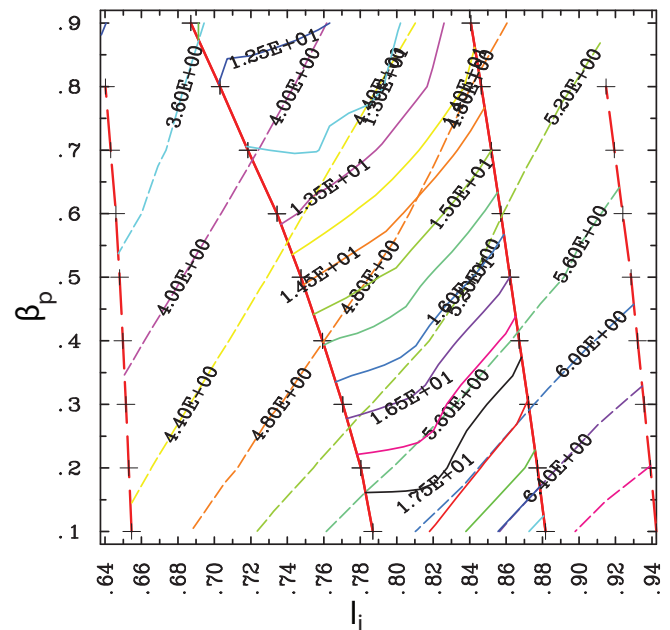


FIG. 5: Contours (in the achievable operating space illustrated in Fig. 4) of the vertical-instability growth-rate γ for both baseline (dashed) and elevated (solid) strike-point configurations (14 MA H-mode).

lower current is easier since coil resources do not need to be utilized at full. Also, adjusting the required flux-linkage has a significant effect on the extent of the l_i range.

For 12 MA H-mode, the possible formulations of the constraint sets imposed on the Grad-Shafranov equation to meet our physical constraints become diverse; we identified at least three different specifications which taken together almost cover the entire H-mode operating space. While we investigated only three sets of constraints, there exist many more formulations which overlap with each other (and, we expect, will cover the gaps between the three solutions in Fig. 6). Fig. 7 shows equilibrium shapes (for $\beta_p = 0.8$) in the two regions where the solutions overlap. Fig. 8 and Fig. 9 show corresponding pressure and q profiles (versus minor radius) in those overlapping regions.

The resulting flexibility of solutions which can satisfy a given set of physical constraints facilitates the development of successful vertical control scenarios. It gives freedom to choose additional specifications to achieve additional physics constraints or optimization. It is also promising for the existence of equilibria (including the gap regions in Fig. 6 at moderate β_p and below) compatible with time-dependent current drive and transport, which naturally introduces additional limitations.

In Fig. 6, the solid red line shows the left limit we found in $\beta_p - l_i$ operating space achievable in 12 MA H-mode. In this limit, equilibria are found by constraining the outboard SOL-wall distance to 8 cm and the coil

⁴ Displacements of 4% of the minor radius are at the limit of controllability in ITER using the VS3 system. Using typical noise levels, for which the probability is very high at or below this displacement, this corresponds to a growth rate of about 20 rad/sec [15].

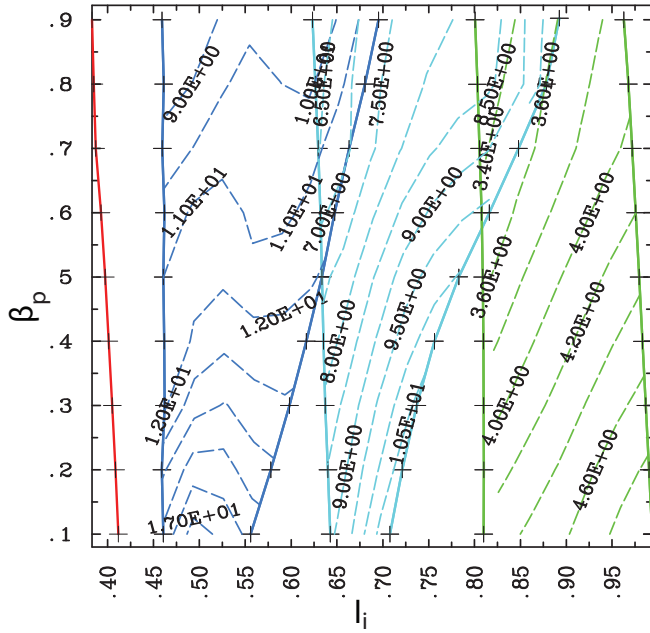


FIG. 6: The contour plot of the vertical-instability growth-rate γ for 12 MA H-mode elevated-strike-point configuration (vertical positions are Z_{el0}^{in} and Z_{el0}^{out}). The first, second and third solution-formulations are shown in **blue**, **cyan** and **green**, respectively.

force (either net or repulsive) to its maximum via varying the radial positions of the first two fixed points; also, we force $\max(U) = 1$ by varying the steepness of the current profile. The resulting equilibria have concave shapes ($d^2 Z/dR^2 < 0$ on average) in the inboard half-plane. By increasing the weights of the fuzzy points in the upper parts of the equilibria, we obtain the lower limit (left solid **blue** line) of the operating space with flat shapes ($d^2 Z/dR^2 = 0$ on average) in the inboard half-plane. As l_i is increased from the lower limit of this first (left **blue** line) solution, $\max(U)$ drops below unity and then again reaches unity, which defines the upper limit (right **blue** line).

For the second solution (**cyan** lines), similarly to the first (but with different constraints; see the Appendix for the details), we force $\max(U) = 1$ (at both lower and upper limits) by varying the steepness of the current profile. For the third solution (**green** lines), the lower limit of the operating space is found when $\max(U)$ reaches unity; the upper limit is found when the balance discussed above for 14 MA occurs between the flattening and peaking of the current on the axis.

For 12 MA H-mode, Fig. 6 also shows the contours of the vertical-instability growth-rate γ for the three solution-sets. The third solution (**green**, found at larger l_i) is more vertically stable than the second one (**cyan**), while the second solution is more stable than the first (**blue**). Within any given solution, however, γ increases with l_i and decreases with β_p , as expected (see below) and as in Fig. 5. Growth rates can vary significantly be-

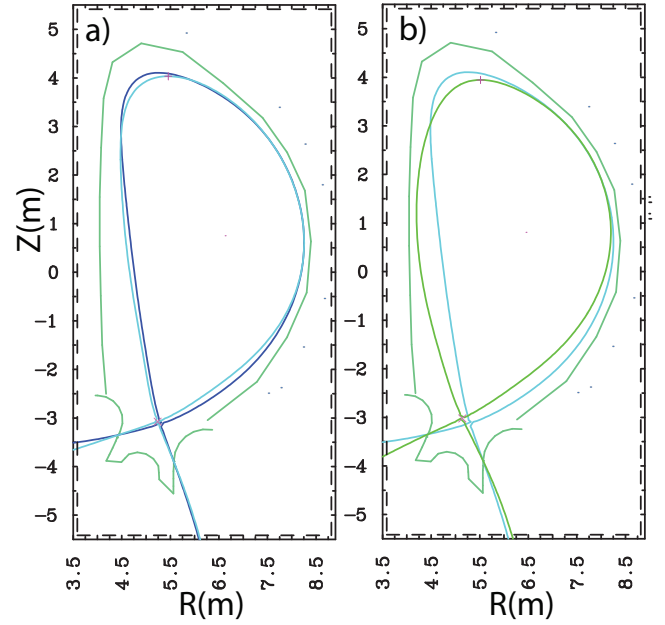


FIG. 7: Equilibrium plasma shapes in the overlapping regions shown in Fig. 6 for $\beta_p = 0.8$. The **blue** and **cyan** separatrixes in (a) are the first and second solutions at $l_i = 0.65$, while the **cyan** and **green** separatrixes in (b) are the second and third solutions at $l_i = 0.85$.

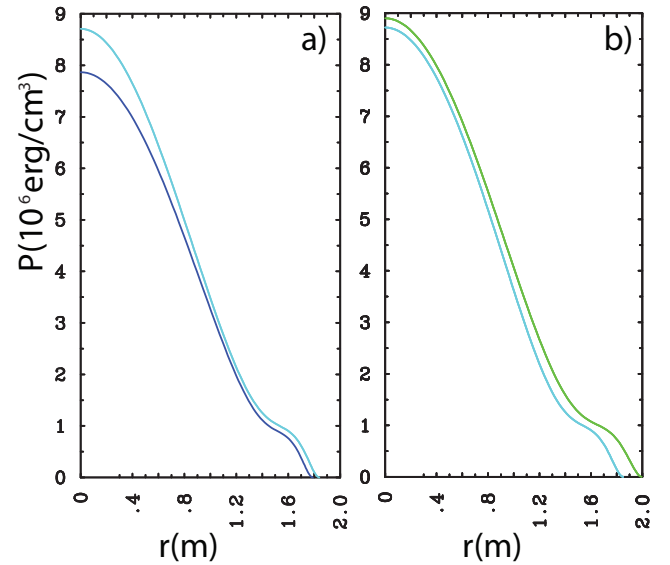


FIG. 8: Pressure profiles vs. minor radius in the overlapping regions shown in Fig. 6 for $\beta_p = 0.8$; l_i is 0.65 and 0.85 in (a) and (b) respectively.

tween different constraint sets. For typical $l_i = 0.85$ and $\beta_p = 0.7$, for the **green** and **cyan** solutions, we found $\gamma = 3.5 \text{ s}^{-1}$ and 9.0 s^{-1} , respectively. For the first solution (**blue**) at fixed β_p , γ does not vary monotonically. This is discussed below.

Fig. 10 shows the contours of the elongation (elon-

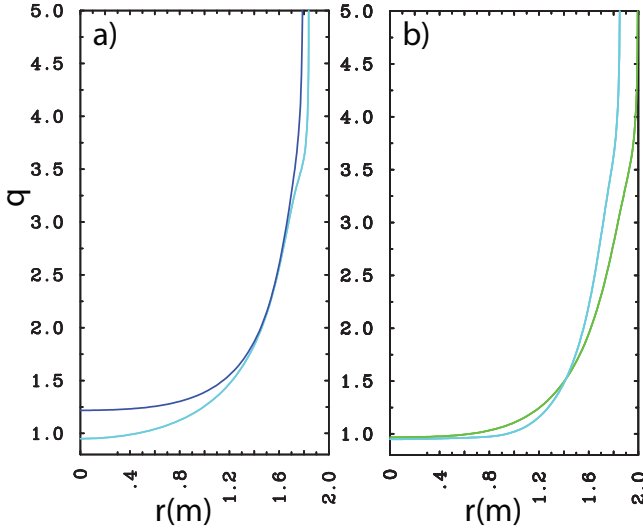


FIG. 9: q profiles vs. minor radius in the overlapping regions shown in Fig. 6 for $\beta_p = 0.8$; l_i is 0.65 and 0.85 in (a) and (b) respectively.

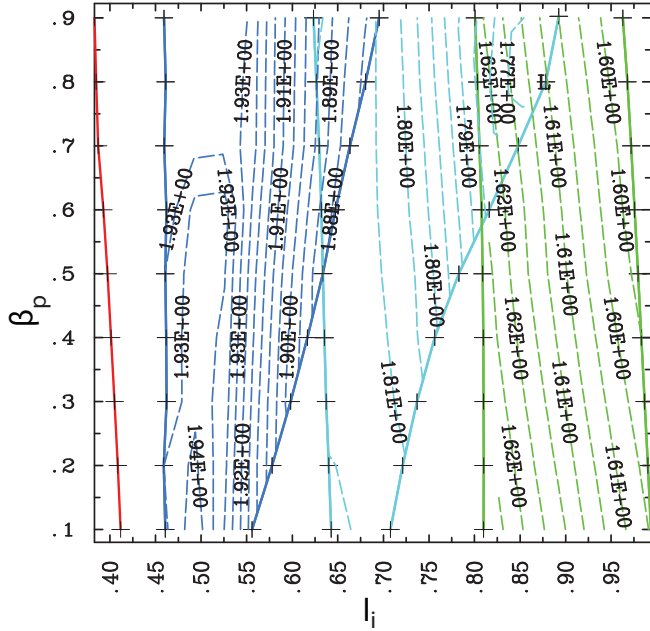


FIG. 10: The contour plot of the elongation for 12 MA H-mode elevated-strike-point configuration.

gation greater than unity drives the instability) for the three solutions. The elongation, from region to region, decreases with l_i , explaining the trend in γ between regions seen in Fig. 6. In the regions of operating space where different solutions overlap, the solution which is more vertically unstable has the more elongated separatrix (see Fig. 7). However it is clear that elongation is not the only factor contributing to the growth rate at a given l_i . For example, by comparing Figs. 6 and 10, for the first

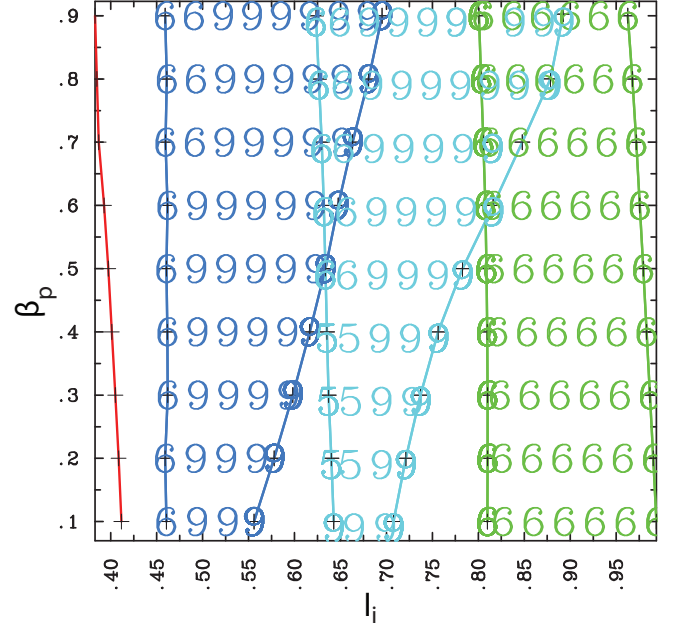


FIG. 11: Schematic figure to illustrate which coil has the maximum utilization factor (12 MA H-mode). Coils PF5 and PF6 are denoted by numbers 5 and 6, while CS1L is denoted by number 9 (see Fig. 2).

solution near $l_i = 0.53$ the elongation is almost constant when varying β_p from 0.1 to 0.9, while the growth rate changes substantially from 17 s^{-1} to 9 s^{-1} . Also, for the first two solutions at $(l_i, \beta_p) = (0.8, 0.65)$, γ is 10.0 s^{-1} and 6.5 s^{-1} , respectively, while the difference in elongations is only slight (1.89 and 1.82, respectively). Similarly, for the last two solutions at $(l_i, \beta_p) = (0.8, 0.85)$, γ is 9.0 s^{-1} and 3.5 s^{-1} , respectively, while the elongation is 1.77 and 1.62, respectively. Also, for the three solutions (at $\beta_p = 0.5$ near the right limits), γ is 12 s^{-1} , 10 s^{-1} and 4.4 s^{-1} , respectively, while the difference in elongations is only slight (1.88, 1.8 and 1.6, respectively).

For fixed plasma shape, in general, the dependence of γ on l_i is due to the effect of changes in the current distribution relative to the passive structure: at higher l_i , the peaking of the current profile moves plasma current further away from the stabilizing vacuum vessel and γ increases. At fixed l_i , γ decreases as β_p is increased; while this needs further investigation, one of the contributing factors might be the Shafranov shift of the equilibrium flux surfaces: the shift increases with β_p and the current moves closer to the vacuum vessel-wall. These and other effects are discussed in [8, 16]. In Ref. 8, an initial drop in γ vs. l_i at low l_i with β_p and elongation fixed was observed. The broader current-profiles at low l_i not only induce increased wall-stabilization; in placing more current at higher elongation, they promote the drive. The latter effect is dominant at low l_i in some configurations. At low l_i , our results in Fig. 6 exhibit yet more complicated variation, with the growth-rate rising, then falling

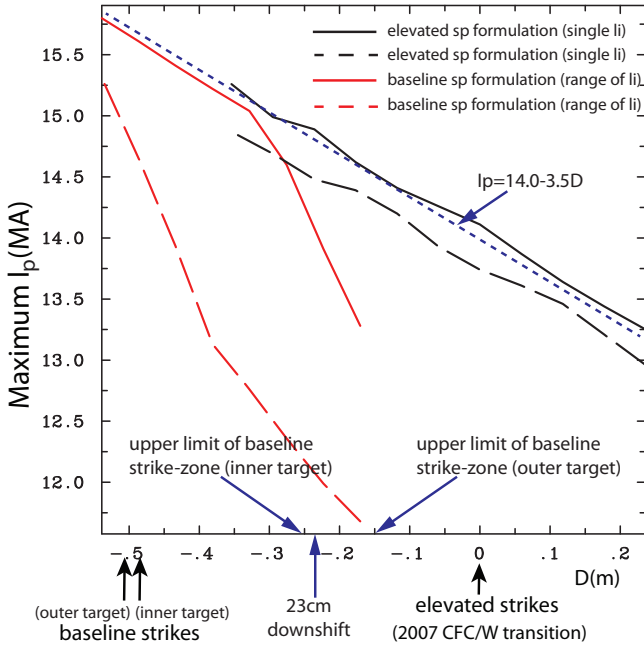


FIG. 12: Maximum achievable H-mode plasma current versus strike-point positions on the divertor plates. The black and red solutions are based on the formulations described in Sec. III A (for elevated and baseline strike-point configurations, respectively). The solid curves are the solutions with a single valid l_i , while the dashed curves are the solutions with a finite range of l_i .

and rising again at fixed β_p as l_i increases. This appears to be correlated with the elongation (Fig. 10); but the elongation varies only slightly over this range of l_i . The competing l_i effects may be playing some role; but we note the non-monotonic behavior of the net CS coil force (see App. A) in this portion of operating space and speculate the low- l_i structure of the growth-rate primarily due to equilibrium geometric adjustments in response to the associated changes in the PF and CS coil currents as l_i is raised.

In these references a drop in γ vs. l_i at low l_i with β_p fixed was observed, as we find at $l_i \sim 0.53$ in Fig. 6. Here, however, the plasma shape is allowed to vary somewhat in the course of satisfying our constraints, and the low- l_i structure is more complicated. The growth-rate first rises and then drops with increasing l_i at fixed β_p . This is correlated with the elongation (Fig. 10), but since the elongation varies only slightly we speculate that the lower- l_i structure of the growth rate is primarily due to plasma-current profile adjustments in response to the non-monotonic behavior of the net CS coil force (see App. A).

Superconducting coil constraints: The coil which most constrains the equilibrium (has the largest U ; i.e., is closest to its superconducting operation limit) depends on where in operating space we are and which solution we are looking at. In Fig. 11, we use coil numbers (see

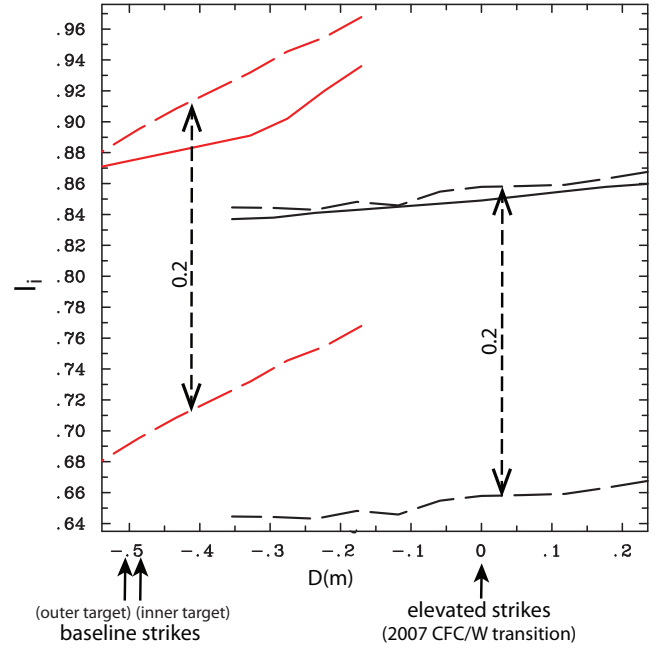


FIG. 13: (Data from the same equilibria as in Fig. 12.) Accessible l_i operating space, with a fixed width of 0.2 (dashed lines), versus strike-point positions on the divertor plates D . The solid line plots l_i at the maximum achievable I_p versus D .

Fig. 2) to show which coil has the maximum U . For the 12 MA H-mode case of Fig. 6, the most constraining coil varies between the PF5, PF6 (shown by 5 and 6) and CS1L (shown by 9) coils. For comparison, for the higher-current (14 MA H-mode) case reviewed above, the most contributing coil is always PF6.

C. Maximum achievable H-mode plasma current as a function of vertical strike-point position

In Fig. 12 we investigate the maximum achievable plasma current I_p^{\max} as the strike-point locations are varied along the divertor plates (for fixed $\beta_p = 0.7$). On the horizontal axis, D is the distance along the divertor plates away from the elevated strike-point positions; both strike-points are shifted by the same distance along the plates. The maximum raised position we consider is 25 cm above the 2007 transition point.

For each D , we follow the two solutions (shown in black and red for the elevated and baseline strike-point 14 MA H-mode constraint-sets, respectively) obtained based on the formulations described in Sec. III A and detailed in the Appendix; I_p was raised until the code failed to find a solution. The two solutions overlap in some interval of D on the divertor plates. This is a result, once again, of there being freedom left in the equilibria after all the physics constraints have been met, so that I_p^{\max} depends on the formulation of the constraints. For an all-W di-

vector, for operation with given strike-point locations, this merely indicates that there is room for further optimization of I_p^{\max} (i.e., that the I_p^{\max} obtained here is achievable by plasmas of various shapes and profiles). The CFC/W divertor is discussed below.

In Fig. 12 the solid lines show I_p^{\max} when all the constraints can be satisfied only at a single $\beta_p - l_i$ point in operating space (for a given strike-point position). The corresponding l_i are shown by the solid lines in Fig. 13. Note that the baseline case allows for up to 15.7 MA operation, while operation with elevated strike-points at $Z_{\text{el0}}^{\text{in,out}}$ allows up to 14.1 MA. The dependence of I_p^{\max} versus D can be approximated by $I_p^{\max}(\text{MA}) = 14.0 - 3.5D(\text{m})$ (dotted line in Fig. 12).

The dashed curves in Fig. 12 show I_p^{\max} for the two solutions when all the constraints are satisfied in a finite interval of l_i . The width of this interval is chosen to be equal to 0.2 (as illustrated by the dashed lines in Fig. 13). This more relaxed approach to determine I_p^{\max} provides contingency in the event of a wider range of experimental plasma self-inductance than originally anticipated [17]. Also, l_i will differ from the values found for the equilibria here, given profiles consistent with transport evolution; and l_i will have a range due to variations in profiles for different operating scenarios.

The divertor strike-line excursion requirement demands that the CFC/W transitions as well as reflector parts (Fig. 1) of the divertor not be in the area within 15 cm and 5 cm in the upward and downward directions (vertically) respectively from the baseline strike-point positions (on carbon in the CFC/W divertor) [9, 12]. In Fig. 12 we show these upward limits of the allowed strike-zones on the inner and outer divertor targets: the transition points must lie to the right of the blue arrows. On W, when there are overlapping solutions for I_p^{\max} , the black solutions require smaller shifts than the red at a given I_p^{\max} , and thus will be the last to violate the strike-line excursion criterion.

According to the result in Fig. 12, then, to allow operation on W in a CFC/W divertor at 15 MA with a single valid l_i or at 14.5 MA with a finite valid range of l_i , the transition points must be shifted downward another 23 cm along each plate from the present design (as demonstrated by the solid and dashed black curves respectively). Note that a such a downshift of the transition points violates the divertor strike-line excursion criterion on the outer divertor target.

Finally we remark on ITER's 17 MA scenario, which might appear from Fig. 12 to be impossible. We note, however, that q_{95} is roughly proportional to $1/I_p$, and we find that simply relaxing the constraint on q_{95} permits higher I_p^{\max} . The low- l_i operating-space limit for the configurations and plasma currents studied in Sec. III was determined by various constraints; in Fig. 4, for example, superconducting and force limits on the coils as well as the q_{95} constraint were each the operative constraint for some low- l_i curve, as detailed in the Appendix. The most constricted space (14 MA H-mode with el-

evated strike-points) was limited by q_{95} . Upon relaxing the q_{95} constraint but otherwise maintaining the full set of physics/engineering constraints, we find that with $q_{95} = 2.75$, $\beta_p = 0.7$, $l_i = 0.84$ and the baseline strike-point positions $Z_{\text{base}}^{\text{in,out}}$, 17 MA H-mode equilibria are possible (using the baseline-strike-point constraint formulation). This is consistent with ITER's 17 MA H-mode scenario [13].

Further explorations, e.g., varying the constraint formulations and applying different shifts on the inner and outer targets, could be undertaken to increase I_p^{\max} for a given D . The strategy for specifying the plasma shape could be changed; e.g., drop all reference to the 15 MA baseline shape in favor of specifying elongation, triangularity, lower X-point location, etc.

IV. CONCLUSIONS

We investigated the range of possible Start-of-Burn ITER H- and L-mode equilibria with elevated strike-points. For the present divertor design, for operation with raised strike-points (roughly at the 2007 CFC/W transitions), the maximum achievable plasma current is about 14 MA. While at 14 MA these elevated strike-points lead to significant reduction of H-mode $\beta_p - l_i$ operating space, there is only a slight reduction of space for 12 MA operation. At the lower current, multiple equilibria which meet our constraints have been found. 15 MA (single valid l_i) or 14.5 MA (finite valid range of l_i) operation is possible with the strike-points moved upwards 25.6 cm and 27.6 cm (for the inner and outer divertor plates respectively) along the divertor from their present baseline strike-point locations. For a CFC/W divertor, such a shift would violate the divertor strike-line excursion criterion on the outer divertor target (the transition point must be at least 15 cm away in the upward direction from the baseline strike-point).

Vertical-instability growth-rates for the raised strike-point configuration at high-current (14 MA) H-mode operation were assessed and found to be within the limit of controllability using the VS3 system (in-vessel copper coil pair 13 and 14 in Fig. 2). For 14 MA L-mode and 12 MA operation, γ is well within the limit. At 12 MA, where multiple formulations of the constraints are possible at given β_p and l_i , the growth rate varies significantly (remaining within the limit) depending upon which solution we look at at a given point in operating space. We note, however, that in satisfying the wall-clearance and dR_{sep} constraints we have not taken into account finite vertical excursions initiating vertical-displacement events. Assessment of the critical disturbance size that meets the geometric constraints or, alternatively, modifying the constraints to allow for a given excursion of the magnetic axis, remains for future studies.

The multiplicity of solutions seen in Fig. 6 for 12 MA (and which would also occur below 12 MA, of course) indicates there is some freedom to choose constraints

to achieve various additional goals. Also, the multiplicity indicates that over much of the operating space, the existence of equilibria satisfying our physics constraint set does not require very tight profile control, which should ease the development of scenarios and the ability to achieve them experimentally at the plasma currents we give here. Given this flexibility, it is clear that the limits and growth rates found in this paper should not be regarded as absolute from the equilibrium point of view (see the discussion of 14 MA L-mode at low l_i with baseline strike-points in Fig. 4 for an example). However, we do not expect further exploration with alternate formulations meeting our constraints on coils, q_0 , q_{95} , etc., to significantly expand the operating space we have found for elevated strike-points, particularly at 14 MA. On the other hand, at lower plasma currents, different formulations could have an impact on plasma shape and coil-currents and lead to more significant effects. Also, relaxing the constraints on q_0 and q_{95} (lowering the minimum required values) will expand l_i operating space at the high and low ends, respectively. Asymmetric shifts of the strike-points on the inner and outer targets could also be considered in future optimization studies. Finally, we note that the results presented here also do not include the effects of non-axisymmetric instabilities. These will certainly reduce the accessible operating space. The results presented in this paper provide a first assessment of the $\beta_p - l_i$ operating-space limits imposed by the ITER coil set as a function of divertor-strike-point location. The equilibria can serve as a starting point for the more detailed scenario studies including time-dependent studies of position and shape control, current drive and transport, stability, and edge dynamics (such as particle and heat exhaust in the divertor area) required to investigate the exact operating space possible for given strike-points.

APPENDIX A

The detailed information about input parameters used in our simulations is collected in this appendix to help reproduce the results presented in the paper as well as to record our experience with strategy which may be of use in future equilibrium studies.

In Fig. 4, to obtain the *14 MA H-mode elevated-strike-point equilibria*, we started with the baseline 15 MA SOB ITER solution with baseline β_p (0.7) and l_i (0.85) and originally located strike-points. The current was changed to 14 MA while the initial flux Ψ_{init} was adjusted to 92 Wb. Also, the following conditions are satisfied:

- Two of the four fixed points (points 3–4 in Fig. 3) are positioned on the vertical divertor plates to ensure elevated strike-points at (4.433 m, -3.35 m) and (5.572 m, -3.90 m) in the (R, Z) plane. The other two fixed points (points 1–2 in Fig. 3) are positioned axially at 0.569 m, while their radial positions are varied to constrain the minimum distances

between the SOL and the first wall in the outboard and inboard half-planes to be equal to 8 cm;

- To enforce the condition that the SOL lie within the inactive separatrix, dR_{sep} is constrained to be 4.05 cm (this is done for convenience).
- With the total number of fuzzy boundary points being 61, points 23–37 (between the first fixed-point and the upper part of the separatrix) are assigned to have weights equal to 0.25, with the rest having zero weights. In the simulation the fuzzy points with bigger weights are given higher priority in the least-squares matching procedure. If the weights are too big, the solution might not be found since the problem would be overconstrained (the number of parameters which can be varied is finite). If the weights are too small, some constraints (such as SOL-wall distance and dR_{sep}) might be easily violated. The sum of the squared coil currents is minimized in the least-squares sense;
- The steepness of the current profile a_J [Eq. (3)] is varied to constrain l_i . The multiplier β_J on the pressure profile [Eq. (4)] is varied to constrain β_p ;
- The current in PF6 coil is varied to constrain $f = 1$.

The left and the right limits of the operating space (solid red lines) for H-mode elevated-strike-point configuration are found when $q_{95} = 3$ and $a_J = 10$ are satisfied (see Sec. III A for detailed discussion), respectively.

The *14 MA L-mode elevated-strike-point equilibria* (between solid blue lines) are determined the same way—and the right limit determined by the same constraint—as described above for the H-mode. The left limit is found when $q_{95} = 3$ for $\beta_p \leq 0.3$ and the net CS coil force is equal to its maximum (60.0 MN) for $\beta_p \geq 0.4$. Also dR_{sep} is constrained to be 4.81 cm. (For the rest of the equilibria described below constraining dR_{sep} is unnecessary since $dR_{\text{sep}} \geq 4$ cm is naturally satisfied.)

In Fig. 4, to obtain the *14 MA H-mode baseline strike-point equilibria*, we started with the baseline 15 MA SOB ITER solution with β_p (0.7) and l_i (0.85) and originally located strike-points. The current was changed to 14 MA while the initial flux Ψ_{init} was adjusted to 92 Wb. Also, the following conditions are satisfied:

- Fixed points 1–2 are positioned on the vertical divertor plates to ensure baseline strike-points at (4.226 m, -3.79 m) and (5.565 m, -4.406 m) in the (R, Z) plane. Fixed points 3–4 are positioned axially at 0.569 m and their radial positions are varied to constrain the baseline size specification for the plasma (major and minor radii are 6.2 and 2.0 m respectively), while the SOL-wall distance is ensured to be at least 8 cm;
- With the total number of fuzzy boundary points being 61, all points are assigned to have weights

equal to 16. The sum of the squared coil currents is minimized;

- The steepness of the current profile a_J [Eq. (3)] is varied to constrain l_i . The parameter β_J is varied to constrain β_p ;
- The current in PF6 coil is varied to constrain $f = 1$;
- The sawtooth flattening region x_s is varied ($x_s \geq 0$) to constrain $q_0 \geq 0.95$.

The left and the right limits of the operating space (dashed red lines) for H-mode baseline strike-point configurations are found when $\max(U) = 1$ and $a_J = 10$ are satisfied, respectively.

The 14 MA *L-mode baseline strike-point equilibria* (between the dashed blue lines) are determined the same way as described above for the H-mode, except the constraint on f is removed. The left limit is found when $\max(U) = 1$ is satisfied. At high l_i the right limit is defined as $l_i = 1$ for simplicity, since the conflicting needs of peaking the current profile (increasing a_J) to increase l_i while flattening in the center (increasing x_s) to constrain q_0 lead to a square-like profile that causes numerical problems and in the end is not realistic.

In Fig. 6, to obtain the left limit (solid red line; with concave shapes: $d^2Z/dR^2 < 0$ on average) of the operating space for the 12 MA *H-mode elevated-strike-point configuration*, we started with the above-described elevated-strike-point 14 MA SOB ITER solution with baseline β_p (0.7) and l_i (0.85). The current was changed to 12 MA while the initial flux Ψ_{init} was adjusted to 64 Wb. Also, the following conditions are satisfied:

- Fixed points 1–2 are again positioned on the vertical divertor plates to ensure elevated strike-points at (4.433 m, -3.35 m) and (5.572 m, -3.90 m) in the (R, Z) plane. Fixed points 3–4 are positioned axially at 0.569 m, while their radial positions are varied to constrain the minimum outboard SOL-wall distance to be equal to 8 cm and either the net or repulsive CS coil force to its maximum (either 60 MN or 120 MN), with the other force then below its limit;
- With the total number of fuzzy boundary points being 125, points 48–88 (between the first fixed-point and the upper part of the separatrix) are assigned to have weights equal to 0.3125, with the rest having zero weights. The sum of the squares of the magnetic field at the coils is minimized;

- The parameter a_J is varied; and $\max(U)$ is constrained to be unity. The parameter β_J is varied to constrain β_p . l_i is allowed to float.

By increasing the weights of the fuzzy points 48–88, we obtain the lower limit (left solid blue line) of the operating space with flat shapes in the inboard half-plane. Starting with this flat solution, we replace the $\max(U)$ constraint with the l_i constraint. The repulsive CS force is now constrained to its value on the lower limit line; this replaces the previous CS coil force constraint. As l_i is increased away from the lower limit line, $\max(U)$ drops below unity and then again reaches unity, which defines the upper limit (right blue line). As l_i is increased, the net SC coil force behaves non-monotonically; when this force tries to exceed its maximum value, it is constrained to be equal to this value (again by replacing the previous CS coil force constraint).

The second solution (cyan lines) is found by constraining the outboard SOL-wall distance to 8 cm and minimum radial plasma position to 4.476 m via varying the radial positions of the first two fixed points. Also, the sum of the squares of the coil currents is minimized. Similarly to the first solution, $\max(U)$ is forced to unity (at both lower and upper limits) by varying the steepness of the current profile a_J .

The third solution (green lines) is found by constraining the baseline size specification for the plasma (major and minor radii are 6.2 and 2.0 m, respectively) via varying the radial positions of the first two fixed points; the SOL-wall distance is ensured to be at least 8 cm. The lower limit of the operating space is found when $\max(U) = 1$; the upper limit is found when the balance occurs between the flattening and peaking of the current on the axis.

ACKNOWLEDGMENTS

The authors would like to thank L. D. Pearlstein and Y. Gribov for useful comments and criticisms. We would also like to thank our referees for their carefulness and their many useful observations and suggestions.

This work was performed under the auspices of the U.S. Department of Energy by Lawrence Livermore National Laboratory under Contract DE-AC52-07NA27344.

The views and opinions expressed herein do not necessarily reflect those of the ITER Organization.

[1] R. A. Pitts, A. Kukushkin, A. Loarte et al., Phys. Scr. **T138**, 014001 (2009).
 [2] R. A. Pitts, S. Carpentier, F. Escourbiac et al., J. Nucl. Mater. **438**, S48 (2013).

[3] B. Lipschultz, J. W. Coenen, H. S. Barnard et al., Nuclear Fusion **52**, 123002 (2012).
 [4] J. W. Coenen, V. Philips, S. Brezinsek, et al., Nuclear Fusion **51**, 083008 (2011).

- [5] J. A. Crotinger et al., CORSICA: a comprehensive simulation of toroidal magnetic-fusion devices, LLNL Technical Report UCRL-ID-126284, (1997).
- [6] L. L. LoDestro and L. D. Pearlstein, *Phys. Plasmas* **1**(1), 90 (1994).
- [7] D. A. Humphreys, T. A. Casper, N. Eidietis et al., *Nuclear Fusion* **49**, 115003 (2009).
- [8] S. W. Haney, L. D. Pearlstein, R. H. Bulmer, J. P. Freidberg, *Plasma Physics Reports* **23**, 789 (1997).
- [9] Y. Gribov, ITER Organization, private communication, 2010-12-14.
- [10] S. Ejima, R. W. Callis, J. L. Luxon et al., *Nuclear Fusion* **22**, 1313 (1982).
- [11] G. L. Jackson, T. A. Casper, T. C. Luce et al., *Nuclear Fusion* **49**, 1 (2009).
- [12] R. H. Bulmer, ITER Fiducial Equilibrium States. <http://wormhole.ucllnl.org/caltrans> (2010).
- [13] Y. Gribov, ITER Organization, private communication, 2013.
- [14] R. H. Bulmer, Modeling ITER Resistive Coils in Corsica. <http://wormhole.ucllnl.org/caltrans> (2010).
- [15] D. A. Humphreys, General Atomics, private communication, 2012.
- [16] D. J. Ward, A. Bondeson, F. Hofmann, *Nuclear Fusion* **33**, 821 (1993).
- [17] A. C. C. Sips, T. A. Casper, E. J. Doyle et al., *Nuclear Fusion* **49**, 085015 (2009).